

Nonlinear edge localized mode with impurity seeding in CFETR hybrid scenario

Shiyong Zeng

State Key Laboratory of Advanced Electromagnetic Technology, International Joint Research Laboratory of Magnetic Confinement Fusion and Plasma Physics, School of Electrical and Electronic Engineering, Huazhong University of Science and Technology, Wuhan, Hubei 430074, China

Ping Zhu

State Key Laboratory of Advanced Electromagnetic Technology, International Joint Research Laboratory of Magnetic Confinement Fusion and Plasma Physics, School of Electrical and Electronic Engineering, Huazhong University of Science and Technology, Wuhan, Hubei 430074, China

Department of Nuclear Engineering and Engineering Physics, University of Wisconsin-Madison, Madison, Wisconsin 53706, USA

E-mail: zhup@hust.edu.cn

27 June 2025

Abstract. A critical challenge for operating fusion burning plasma in high-confinement mode lies in mitigating damage caused by edge localized modes (ELMs). While impurity seeding has been experimentally validated as a reliable and effective ELM mitigation technique, its underlying physics remains insufficiently understood and requires further clarification. Through nonlinear magnetohydrodynamic (MHD) simulations, this work reproduces key features of natural ELM crash and reveals its trigger mechanism. Impurity seeding significantly affects nonlinear ELM dynamics by inducing local and global modifications to the pedestal pressure profile, driving high- n ballooning mode instabilities that govern ELM crash. Two critical control parameters—impurity density level and poloidal seeding location—are systematically investigated, which play key roles in the ELM crash onset timing and the resulting energy loss magnitude.

1. Introduction

The operation scenario for next-generation tokamaks aiming to achieve fusion burning plasmas fundamentally relies on the high-confinement mode (H-mode) [1], which is characterized by the formation of a narrow transport barrier at the plasma edge. The consequent periodic burst instability at the pedestal region, known as the edge localized mode (ELM), exhibits a dual nature: while preventing impurity accumulation in the plasma core, it concurrently releases intense heat and particle fluxes within milliseconds, posing severe threats to the lifetime of plasma-facing components (PFCs). Experimental data reveal that the crash size of the most hazardous type-I ELM shows strong correlation with pedestal plasma collisionality ν_{ped}^* [2], quantified by $\Delta W_{ELM}/W_{th}$, where ΔW_{ELM} represents the energy loss per ELM crash and W_{th} denotes the plasma stored thermal energy. Projections indicate ELM sizes of approximately 19% ($\Delta W_{ELM} \approx 22$ MJ) in ITER [2] and 17% ($\Delta W_{ELM} \approx 51$ MJ) in China Fusion Engineering Test Reactor (CFETR) plasmas ($\nu_{ped}^* \sim 0.05\ddagger$) [3]. However, engineering constraints mandate $\Delta W_{ELM} < 1$ MJ m⁻² for PFC protection [4]. Substantial progress has been achieved in elucidating ELM physics through systematic investigations [5, 6, 7, 8, 9, 10, 11, 12, 13]. The prevailing paradigm attributes type-I ELM to ideal magnetohydrodynamic (MHD) peeling-ballooning mode (PBM) instabilities [14]. Recent advances reveal that resistive PBMs develop prior to reaching the ideal MHD stability limit when finite plasma resistivity is considered [15, 16], yielding better agreement with experimental observations. Complementary mechanisms—including the nonlinear explosive growth of ballooning modes [17, 18] and three-wave coupling phenomena observed in DIII-D plasmas [19]—offer alternative frameworks for interpreting ELM dynamics.

Building upon the fundamental understanding of natural ELM, extensive research efforts have focused on mitigating type-I ELM by converting large-amplitude/low-frequency crash into small-amplitude/high-frequency event or ELM-free regime, as demonstrated through diverse techniques across multiple devices: including impurity seeding using main ion or noble gas on JET [20], ASDEX Upgrade [21], and EAST [22]; supersonic molecular beam injection (SMBI) on EAST [23], HL-2A [24, 25], and KSTAR [26]; laser blow-off metal injection on HL-2A [27, 28]; lithium granule/boron powder injection on EAST [29, 30, 31]; and pellet injection on DIII-D [32, 33, 34], JET [35, 36], and ASDEX Upgrade [37, 38]. Furthermore, numerical simulations have significantly advanced the understanding of impurity seeding ELM physics [11]. BOUT++ simulations demonstrate quantitative correlations between ELM size and pedestal resistivity [39, 40, 41]. M3D-C1 simulations reveal a pronounced dependence of the pellet mass threshold on poloidal injection location for ELM triggering [42].

\ddagger $\nu_{ped}^* = \epsilon^{-3/2} R q_{95} / \lambda_{e,e}$, where ϵ , R , and q_{95} are the inverse aspect ratio, major radius, and safety factor at the 95% flux surface, respectively. The electron-electron Coulomb collision mean free path length $\lambda_{e,e} = 1.44 \times 10^{23} T_e^2 / (n \ln \Lambda)$ with $\ln \Lambda = 14.9 - 0.5 \ln (n/10^{20}) + \ln T_e$ (units: m, keV, m⁻³) follows the formulation in the appendix of Wesson J. 2011 Tokamaks 4th edn (Oxford: Oxford University Press).

JOREK simulations reproduce multi-ELM cycles using a reduced MHD model [43, 44, 45], incorporating a pellet ablation model that demonstrates localized high-density plasmoid can drive ballooning-type instabilities [46]. Moreover, comparative analyses between natural and pellet triggered ELMs have been conducted [47, 48], and the experimentally observed lag time in pellet triggered ELM has been reproduced [49]. NIMROD simulations demonstrate excellent agreement with ELITE and GATO codes in benchmark studies [50], and enable two-fluid analysis of edge-localized instabilities [51, 52]. Subsequent studies further examine edge current density modulation effects on pedestal stability [53] and provide insights into ELM suppression in lithium-coated NSTX experiments [54]. Additional applications include quantifying enhanced plasma resistivity stabilization effects on peeling-ballooning instabilities in EAST [55] and modeling edge harmonic oscillations in DIII-D Quiescent H-mode discharges [56]. Simulation studies have continuously advanced, such as developing models for kinetic effects that describe turbulent and neoclassical transport in the pedestal region, and creating more complete scrap-off layer/divertor models that incorporate the interaction of neutral particles and plasma.

Despite extensive experimental and simulation advancements, the physics underlying impurity seeding mechanisms for ELM triggering requires further investigation [27, 28, 30, 34, 35, 36, 57]. Previous studies propose that the local plasmoid induced by pellet ablation cloud can reinforce the pedestal pressure gradient, driving ballooning mode instabilities that trigger ELM [32, 33, 38]. However, JOREK simulations indicate that localized pressure gradient enhancement alone cannot fully account for ELM triggering [58]. Lithium coating experiments on NSTX demonstrate significant impacts of entire pedestal profiles [59], with the pedestal density identified as a critical parameter [23, 60]. ASDEX Upgrade experiments further show that outward pedestal density shifts destabilize PBMs, while inward shifts stabilize them [61]. Regarding ELM size-frequency correlations, experiments exhibit reduced ELM size alongside increased frequency, in agreement with the assumption $f_{ELM} \times \Delta W_{ELM} \approx \text{const}$, where f_{ELM} denotes ELM frequency. By contrast, lithium granule injection induces reductions in both ELM size and frequency [29]. Neon impurity fractions exhibit non-monotonic effects on ELM frequency [25], a trend also observed in JET [20].

To advance our understanding on the ELM mitigation via impurity seeding, this study investigates the nonlinear dynamics of ELM with impurity seeding using 3D nonlinear MHD simulations. The effects of impurity seeding—specifically the density perturbations from impurity ionization and the temperature perturbations from radiative cooling—are examined, revealing that impurity induced pedestal density perturbations play a critical role in ELM dynamics under the scenario studied. Two key impurity seeding parameters demonstrating significant impacts on the ELM crash onset and size are systematically analyzed.

The paper is organized as follows: Section 2 introduces the simulation model, the numerical setup, and the equilibrium configuration. Section 3 characterizes the natural ELM crash mechanism and the energy loss in absence of impurity seeding. Section

4 quantifies the impurity density level and poloidal seeding location effects on ELM dynamics. Section 5 gives discussion, and Section 6 summarizes key findings.

2. Simulation model and equilibrium

2.1. Simulation model and setup

The numerical simulations are conducted using the NIMROD code [62]. Our implementation employs a full MHD model that integrates an atomic physics module adapted from the KPRAD code [63, 64]. The governing equations are formulated as:

$$\frac{\partial n_{i,Z}}{\partial t} + \nabla \cdot (n_{i,Z} \mathbf{V}) = \nabla \cdot (D \nabla n_{i,Z}) + S_{ion/rec}, \quad (1)$$

$$\rho \left(\frac{\partial \mathbf{V}}{\partial t} + \mathbf{V} \cdot \nabla \mathbf{V} \right) = -\nabla p + \mathbf{J} \times \mathbf{B} + \nabla \cdot (\rho \nu \nabla \mathbf{V}), \quad (2)$$

$$\frac{n_e}{\Gamma - 1} \left(\frac{\partial T_e}{\partial t} + \mathbf{V} \cdot \nabla T_e \right) = -n_e T_e \nabla \cdot \mathbf{V} - \nabla \cdot \mathbf{q} + Q, \quad (3)$$

$$\mathbf{q} = -n_e [\kappa_{\parallel} \mathbf{b} \mathbf{b} + \kappa_{\perp} (\mathcal{I} - \mathbf{b} \mathbf{b})] \cdot \nabla T_e, \quad (4)$$

$$\frac{\partial \mathbf{B}}{\partial t} = \nabla \times (\mathbf{V} \times \mathbf{B}) - \nabla \times (\eta \mathbf{J}), \quad \mu_0 \mathbf{J} = \nabla \times \mathbf{B}. \quad (5)$$

Here, n_i , n_e , and n_Z denote the main ion, electron, and impurity ion number densities, respectively; ρ , p , and T_e represent the plasma mass density, pressure, and electron temperature; \mathbf{V} , \mathbf{J} , and \mathbf{q} correspond to the velocity, current density, and heat flux; \mathbf{B} is the magnetic field; $\mathbf{b} = \mathbf{B}/B$ defines the unit magnetic field vector; \mathcal{I} represents the unit tensor; $S_{ion/rec}$ denotes the density source; Q corresponds to the energy source; D , ν , η , κ_{\parallel} , and κ_{\perp} characterize the plasma diffusivity, kinematic viscosity, resistivity, parallel and perpendicular thermal conductivity, respectively, and $\Gamma = 5/3$ is the adiabatic index.

The KPRAD module calculates the impurity radiation power with real-time updates of impurity and plasma densities. The energy source term Q comprises contributions from impurity ionization, recombination, line radiation, bremsstrahlung, and Ohmic heating. All particle species adhere to the single-temperature T_e approximation, which assumes instantaneous thermalization across species due to collision timescales being much shorter than the ELM crash timescale τ_{ELM} in the edge pedestal region under impurity seeding. For instance, the electron collision time $\tau_e = 6.4 \times 10^{14} (T_e^{3/2}/Z^2 n_e) \simeq 0.002$ ms $\ll \tau_{ELM} \simeq 0.1$ ms, which are estimated for ion charge number $Z = 5$, $T_e = 2.5$ keV, and $n_e = 5 \times 10^{19}$ m $^{-3}$. Ionization and recombination processes are modeled for both plasma ion and multi-charged impurity ions, with their contributions integrated into the density source term $S_{ion/rec}$. Plasma ions consist of deuterium and are initially fully ionized; neutral deuterium generated via recombination after impurity seeding accounts for only a small fraction of the plasma ion bulk, rendering it negligible. Electron density evolution follows the quasi-neutrality constraint. The plasma pressure p evolves under impurity ionization/recombination and radiative cooling effects, exhibiting pronounced sensitivity to the impurity-induced

modifications of local density and temperature profiles. The initial impurity source is neutral gas and localized near the plasma separatrix, with its quantity increasing linearly over 0.1 ms and featuring Gaussian distributions in both poloidal and toroidal directions (Fig. 1a).

All particle species are assumed to share identical fluid velocity \mathbf{V} , and the plasma is initially stationary ($\mathbf{V}_0 = 0$ m/s). Particle diffusivity $D = 1$ m²/s and viscosity $\nu = 1 \times 10^3$ m²/s are adopted for numerical stability. Thermal conductivities are fixed at $\kappa_\perp = 1$ m²/s and $\kappa_\parallel = 1 \times 10^{10}$ m²/s. The perpendicular thermal conductivity κ_\perp matches the order of experimental values (~ 1 m²/s), whereas the particle diffusivity is one order of magnitude larger than typical experimental values (~ 0.1 m²/s) [65]. Plasma resistivity η follows the Spitzer model: $\eta \propto Z_{\text{eff}} T_e^{-3/2}$, where $Z_{\text{eff}} = 1 + (\sum n_Z/n_e) (\langle Z \rangle^2 - \langle Z \rangle)$, $\langle Z \rangle = (n_e - n_i) / \sum n_Z$ represents the effective charge number incorporating impurity ionization/recombination effects. The numerical implementation employs 40×80 bi-quadratic Lagrange polynomial finite elements in the poloidal plane and 22 Fourier modes spanning toroidal mode numbers $n = 0$ –21. The simulation grid is radially non-uniform, with enhanced resolution in the pedestal region. A vacuum region surrounds the plasma, and a perfectly conducting wall boundary condition is imposed at the edge of simulation domain.

2.2. Equilibrium

The plasma equilibrium employed in the simulations is based on the CFETR hybrid scenario with a lower single-null configuration [3]. Key parameters are summarized in Tab. 1, with equilibrium profiles illustrated in Fig. 1(a). The pedestal region exhibits a width of approximately 6 cm at the outboard mid-plane, featuring pedestal height $n_{e,\text{ped}} = 6.5 \times 10^{19}$ m⁻³ and $T_{e,\text{ped}} = 4.7$ keV, where $n_{e,\text{ped}}$ and $T_{e,\text{ped}}$ are the pedestal electron density and temperature, respectively. Both the maximum local and flux-surface-averaged pressure gradients are located at the pedestal center. The steep pedestal pressure profile induces substantial current density, resulting in reduced magnetic shear and a nearly flat safety factor profile within the narrow pedestal. The large pedestal pressure gradient drives ballooning mode instabilities, while the high current density stabilizes high- n ballooning modes yet destabilizes low- and intermediate- n kink/peeling mode instabilities.

Linear simulations demonstrate that mode growth rates increase monotonically with toroidal mode number n with both ideal MHD conditions and high Lundquist numbers (Fig. 1b). The most unstable high- n modes indicate that ballooning-type instabilities play a dominant role in the ELM crash dynamics for this scenario. Subsequent nonlinear simulations employ high Lundquist numbers ($S \geq 1 \times 10^7$), where notably, the mode growth rates exhibit minimal variation across this regime. In low Lundquist number regimes, elevated plasma resistivity boosts growth rates and shifts down the mode number of the dominant instability. Plasma resistivity can be enhanced after impurity seeding through radiative cooling and ionization processes, thereby modifying MHD

Table 1: Key parameters of the equilibrium

Parameter	Symbol	Value	Unit
Minor radius	a	2.205	m
Major radius	R_0	7.228	m
Plasma current	I_p	1.267×10^1	MA
Toroidal magnetic field	B_t	6.503	T
Central safety factor	q_0	1.380	Dimensionless
Edge safety factor	q_{95}	6.039	Dimensionless
Central electron temperature	$T_{e,core}$	3.082×10^1	keV
Central electron density	$n_{e,core}$	1.258×10^{20}	m^{-3}
Edge electron temperature	$T_{e,edge}$	2.862	keV

instability growth and the resultant ELM dynamics. However, modifications to the pedestal pressure profile, which primarily arise from the impurity-seeding induced density perturbations, are the focus of this study due to their dominant roles in the nonlinear ELM dynamics (discussed in subsequent sections). This dominance likely stems from the equilibrium pedestals that are pressure-gradient-limited, with ballooning-type modes prevailing in the instability spectrum. Whereas plasma resistivity plays a secondary role here, it may gain significance in scenarios where pedestal stability is governed by kink/peeling mode instabilities or in low Lundquist number regimes, thus warranting further investigations.

3. Nonlinear dynamics of natural ELM crash

This section demonstrates the dynamics of a natural ELM crash without prior impurity seeding in terms of filamentary structures, mode structures, the correlation between MHD instabilities and ELM triggering, as well as pedestal collapse and energy loss during the ELM crash. The modes grow from minimal initial seed perturbations, progressing through three distinct stages as illustrated in Fig. 2. Initially, the seed perturbations decay upon simulation onset, with the $n = 1$ mode undergoing an extended decay period. Subsequently, the modes transition into a rapid exponential growth phase, during which the $n = 21$ mode becomes dominant. In the final stage, the modes approach saturation. The growth of the $n = 21$ mode correlates closely with the dynamics of the ELM crash—specifically its saturation time and amplitude. This relationship will be discussed in detail in subsequent sections. All modes remain localized in the pedestal region, with the $n = 21$ mode’s peak positioned near the pedestal waist region at the ELM crash onset (Fig. 3a). Furthermore, the $n = 21$ mode exclusively localizes on the outboard bad-curvature side, in agreement with the ballooning mode instability characteristics (Fig. 3b). The ELM crash and pedestal collapse follow the exponential mode growth during the second stage, manifested by filamentary structure development shown in Figs. 4(a1-a4). The filamentary structures’

spatial patterns resemble those of ballooning-type instabilities, both localized on the bad-curvature side. The pedestal collapse commences at $t = 0.45$ ms, initiating at the pedestal top. The density profile collapses and extends beyond the plasma separatrix due to ballooning-interchange convective cells on the bad-curvature side (Fig. 4b). In contrast, the temperature profile collapses inward with negligible separatrix extension (Fig. 4c), a result attributable to the rapid parallel thermal transport along open field lines outside the plasma separatrix. After $t = 0.55$ ms, the collapse of plasma profile propagates inward following the complete pedestal destruction. In absence of external heating or particle fueling, plasma profiles undergo irreversible collapse once the ELM crash begins. However, the outward fluxes released from the central plasma profile collapse partially restore the pedestal profiles, which is evident in the $t = 0.65$ ms profiles in Figs. 4(b) and (c). The general ELM dynamics outlined above agrees well with experiments. For example, the characteristics of the filamentary structure are consistent with MAST experimental observations [6, 66]. Additionally, precursors with high- n mode number are widely observed to be localized in the pedestal region and grow up before ELM onset [10]. On KSTAR, ELM evolution is also characterized in three stages: initial linear phase, quasi-steady state, and crash phase [67].

To quantify ELM energy loss, Fig. 5 compares the ELM losses calculated using two alternative definitions. The pedestal ELM loss $\Delta W_{ped}/W_{ped,0}$ increases rapidly after $t = 0.45$ ms, peaking at $t = 0.575$ ms upon complete pedestal loss, releasing approximately 50% of the pedestal stored thermal energy. The subsequent decrease results from core plasma fluxes gradually replenishing the pedestal. In contrast, the total ELM loss $\Delta W_{th}/W_{th,0}$ increases monotonically throughout the simulation due to continuous profile collapse, as its calculation encompasses the entire plasma region. For subsequent analysis, the pedestal ELM loss $\Delta W_{ped}/W_{ped,0}$ is adopted as the size of ELM crash, due to its more direct correlation with the pedestal collapse. The rapid increase of the pedestal ELM loss marks the onset of an ELM crash at $t = 0.45$ ms, and its peak at $t = 0.575$ ms is designated as the end of the crash phase. Notably, the total ELM loss $\Delta W_{th}/W_{th,0}$ reaches approximately 6.8% at $t = 0.575$ ms, significantly lower than the experimental scaling prediction ($\sim 17\%$) [2], where the experimental stored energy $W_{th,0}^{exp}$ is estimated using $W_{th,0}^{exp} = 3(n_{e,ped}T_{e,ped})V_{plasma}$ with pedestal density $n_{e,ped}$ and temperature $T_{e,ped}$. By comparison, in simulations the total stored energy $W_{th,0}$ integrates over entire plasma profiles, implying that the experimental scaling prediction likely overestimates ELM size due to an under-estimated $W_{th,0}^{exp}$ in denominator. Despite this discrepancy, approximately 40 MJ of thermal energy is released at $t = 0.575$ ms, posing severe challenges to PFCs.

The $n = 21$ mode acts as the primary driver for the ELM crash, while other modes exert secondary influences (Fig. 6a). The $n = 21$ mode is the most unstable mode at $t = 0.45$ ms when rapid pedestal collapse begins, and approaches saturation by the end of ELM crash. Additionally, the growth of low- and intermediate- n modes undergoes a sudden increase at the onset of pedestal collapse ($t = 0.45$ ms). The $n = 21$ mode, predominantly driven by the pedestal pressure gradient, demonstrates a

coupled interaction with the pressure profile evolution (Fig. 6b). The steep pressure gradient sustains the exponential mode growth prior to ELM crash. Subsequently, the mode growth rate decelerates and transitions into a slowdown phase concurrently with the decreasing pressure gradient (as indicated by the interval between vertical magenta and black lines in Fig. 6b). The mode ultimately enters a secondary steady-growth phase after the pedestal pressure gradient drops to its minimum at $t = 0.575$ ms. Moreover, the pedestal current density evolves similarly as the pressure gradient, presumably contributing to the growth of the peeling mode components. After $t = 0.575$ ms, partial pedestal recovery due to the outward flux of core thermal energy elevates both the pressure gradient and current density, driving renewed growth of the $n = 21$ mode and other modes rather than sustained saturation.

During the ELM crash, the magnetic field lines in the pedestal region become stochastic and spread inward, whereas the plasma profiles collapse simultaneously (Figs. 7). The energy loss dominated by temperature change ΔT_e accounts for the majority of total ELM energy loss evolution (Fig. 8a). This dominance is likely due to rapid thermal transport facilitated by the stochastic magnetic field lines. Released heat flux reaches the wall, resulting in a heat load distribution concentrated at both lower and upper divertors, with peak intensity at the lower divertor (Fig. 8b). However, the simulation results provide only preliminary insights into ELM crash energy loss. A comprehensive understanding of this process requires implementing advanced thermal transport models and incorporating neutral dynamics in the cold, dense scrap-off layer, which both lie beyond the MHD model intended for the limited scope of this study.

4. The influences of impurity seeding on ELM dynamics

This section examines the nonlinear ELM crash process under various impurity seeding scenarios. Compared to the natural ELM crash scenario, impurity seeding can have substantial impacts on the ELM dynamics. Two key control parameters, specifically the impurity density level and the poloidal seeding location, are systematically studied here.

4.1. The density level of impurity seeding

Fig. 9(a) shows ELM crashes under various impurity density levels, with impurities seeded at the outboard mid-plane. Compared to the reference case without impurity seeding, impurity seeding with higher impurity density levels accelerates ELM crash onset and reduces the subsequent ELM size. The $n = 21$ mode remains the most unstable toroidal component across all cases (Fig. 9b1). However, during the early stage it rapidly grows in impurity seeding cases but decays in the reference case. The ELM size $\Delta W_{ped}/\Delta W_{ped,0}$ reaches its peak simultaneously with that of the $n = 21$ mode's growth, and the maximum ELM size scales with the peak amplitude of the mode (Fig. 9b2). After the peak, the growth of the $n = 21$ mode is sustained by partial

pedestal recovery. Additionally, impurity radiation cooling contributes negligibly to the total energy loss. For instance, in the ‘High’ impurity density level case, radiation losses account for only approximately 1.5% (0.7 MJ) of the 46 MJ total thermal energy loss.

Impurity seeding at the plasma separatrix modifies the pedestal plasma pressure profile, inducing a bump at the pedestal foot that amplifies with higher impurity density levels (Fig. 10a). On the one hand, this perturbation shifts the pressure profile outward and enhances the local pressure gradient at the outboard mid-plane pedestal foot, and such effects intensify at higher impurity density levels (Fig. 10b). On the other hand, the enhanced pressure at the pedestal foot mitigates the steep gradient at the pedestal waist, thereby reducing the maximum flux-surface-averaged pedestal pressure gradient at that pedestal location. Higher impurity density levels amplify this reduction (Fig. 10c). Consequently, these impurity seeding induced pedestal pressure perturbations primarily govern the $n = 21$ mode growth and ELM dynamics. The observed correlation between the higher impurity density and the faster ELM crash onset originates from the accelerated early-stage mode growth ($t < 0.1$ ms in Fig. 9b1). Earlier mode saturation enables earlier ELM triggering, as exponential growth rates remain comparable across cases. The rapid initial growth ($t < 0.1$ ms) is driven by the enhanced local pressure gradient during impurity density ramping, with higher impurity density levels leading to earlier growth (Fig. 10b). In contrast, in early stage the mode decays in the reference case, where the impurity induced perturbations are absent. The $n = 21$ mode’s exponential growth rate is proportional to the maximum flux-surface-averaged pressure gradient in the pedestal region, a parameter that decreases with increasing impurity density (Fig. 10c and Fig. 11). Therefore, higher impurity density levels suppress the exponential growth rate, yielding smaller mode amplitude peaks and ELM sizes.

Numerous experiments demonstrate that the amount of injected material plays a critical role in ELM dynamics, where higher impurity densities increase ELM frequency with reduced ELM size. For example, this trend is observed in pellet ELM pacing experiments on DIII-D [32, 33], JET [36] and ASDEX-Upgrade [37], and SMBI impurity seeding experiments on HL-2A [24]. The simulation results are consistent with these experimental findings.

4.2. The poloidal location of impurity seeding

Fig. 12(a) compares the ELM crashes with various poloidal impurity seeding locations, and the initial impurity density level remains identical across all cases. Both the ELM crash onset time and the resulting ELM size $\Delta W_{ped}/\Delta W_{ped,0}$ depend strongly on the poloidal seeding location. The ‘LFS’ impurity seeding triggers ELM crash most effectively, resulting in the fastest crash, whereas the ‘HFS’ seeding delays the crash the most. Moreover, the ‘Top’ and the ‘Bot’ seeding trigger ELM crash at similar time. The ‘Top’ seeding yields the smallest ELM size, whereas the ‘Bot’ seeding produces the largest. Despite variations in nonlinear ELM dynamics, the $n = 21$ mode remains the most unstable mode and shows a strong correlation with the ELM crash evolution (Fig.

12b). The ELM size peak aligns well with the mode's amplitude peak in time across all cases. Furthermore, the maximum ELM size generally scales with the amplitude of this peak, except for the 'Bot' and the 'Top' seeding cases.

The 'Bot' impurity seeding leads to the largest ELM size, indicating that the corresponding saturation peak of the $n = 21$ mode should be the highest. Whereas the $n = 21$ mode growth is primarily driven by the pedestal pressure gradient (e.g., the 'Bot' seeding case; Fig. 13a), the 'Bot' seeding case develops a strong flow that exceeds those from other seeding locations at the time of maximum ELM size (Fig. 13b). This intense flow and its associated shear likely suppress the mode growth rate and reduce the peak amplitude. Furthermore, sheared toroidal rotation is known to stabilize PBMs [68], and similar flow dynamics has been found in JOREK simulations [69]. The largest ELM size in the 'Bot' case is linked to its impurity injection location. Compared to other locations, the 'Bot' seeding at the lower X-point in this single-null plasma configuration induces stronger separatrix perturbations, thereby enhancing confinement degradation. This is corroborated by the largest density loss in the 'Bot' case during the initial 0–0.1 ms phase of impurity density ramping (Fig. 14a), as well as the pedestal temperature drop during the ELM crash (Fig. 14b). Additionally, the pedestal density increase during the crash stems mainly from the outward core plasma fluxes (Fig. 14a). The smallest ELM size observed in the 'Top' seeding case can be explained with the mode growth. While the $n = 21$ mode remains dominant in all cases (e.g., the 'Bot' seeding case; Fig. 15b), its dominance diminishes in the 'Top' seeding case (Fig. 15a). A single dominant high- n mode growth causes more intense perturbations across a broader plasma edge region (Fig. 16b). These perturbations lead to the development of adjacent and significantly overlapping multiple island-chain structures in the edge temperature, which are likely the outcome of magnetic field line stochasticity, thereby facilitating ELM energy loss. In contrast, high- n mode growth is suppressed in the 'Top' case, with subsequent perturbations limited in scope (Fig. 16a). This suppression probably stems from mode competition among growth-comparable modes, resulting in reduced ELM size. Besides, both the 'Top' and 'Bot' cases exhibit an initial transient peak affecting high- n modes ($n \geq 12$), which originates from early-stage density perturbations (Figs. 15).

The growth of the $n = 21$ mode, primarily driven by impurity modified pedestal pressure profile, plays the central role in ELM crash onset for the 'LFS' and the 'HFS' impurity seeding cases (Fig. 17a). In both cases, impurity seeding enhances the local pedestal pressure gradient during the initial 0.1 ms of impurity density ramping (Fig. 17b). The 'LFS' seeding localizes pressure perturbations on the bad-curvature side, directly destabilizing ballooning mode instabilities. Conversely, the 'HFS' seeding induces perturbations on the good-curvature side with a delayed early-stage growth (Fig. 17a). Notably, if the mode's exponential growth rate persists until saturation (dashed line in Fig. 17a), the 'HFS' seeding would trigger earlier ELM crash than the reference case. However, a secondary stagnation phase develops in the 'HFS' case between $t = 0.3$ and 0.4 ms, coinciding with a localized pressure profile peak developed in the pedestal

region (Fig. 17c). The mode resumes exponential growth after the mitigation of this peak, and the growth continues until saturation. This pressure profile peak reduces the maximum flux-surface-averaged pedestal pressure gradient, thereby suppressing the exponential mode growth. The ‘HFS’ seeding induced pressure peak arises from deeper impurity penetration and subsequent ionization, probably due to the inward shift of the local dense perturbations on the high-field side. Similar deep penetration effects are also observed in ASDEX Upgrade experiments and are attributed to toroidal curvature effects [70].

5. Discussion

In DIII-D experiments, outboard mid-plane pellet triggered ELMs exhibit lower energy loss compared to those triggered by the X-point pellet injection [33], in agreement with the ‘LFS’ and the ‘Bot’ impurity seeding simulation results reported here. JET experiments demonstrate that the vertical high-field side (near the device top) pellet injection achieves higher ELM triggering probability than outboard mid-plane injection [36, 71]. Our simulations find that the ‘Top’ seeding delays ELM crash relative to the ‘LFS’ seeding. However, higher ELM triggering probability does not necessarily correlate with faster ELM crash. Systematically exploring ELM triggering efficiency across a broad range of impurity injection locations remains experimentally challenging due to spatial constraints on impurity seeding. JOREK simulations indicate enhanced ELM triggering from the high-field side compared to the low-field side when considering ballooning modes only without peeling-ballooning coupling [58]. In contrast, nonlinear M3D-C1 simulations identify the outboard mid-plane as the most effective location for ELM triggering, with lower/upper X-point regions being least favorable [42]. Compared to those studies, our findings suggest the outboard mid-plane as the optimal impurity seeding location for ELM triggering. Ultimately, impurity seeding location emerges as a critical parameter for ELM mitigation, though definitive conclusions remain elusive due to variations in impurity seeding models and plasma equilibrium scenarios across studies, warranting further investigation.

JOREK multi-ELM cycle simulations reveal that the first ELM crash, initiated by arbitrary seed perturbations, exhibits larger energy loss than subsequent crashes driven by self-consistent perturbations [43, 44]. This occurs because the initial equilibrium is more susceptible to PBM instabilities than later pre-ELM profiles, as the plasma struggles to fully recover its initial state in simulations. Consequently, the energy released during the first ELM crash provides an upper limit for evaluating ELM mitigation strategies. The single-ELM simulations studied here represent this most hazardous scenario. Furthermore, determining the maximum achievable impurity seeded ELM frequency is crucial, since energy per ELM decreases with higher frequency. For example, in the CFETR hybrid scenario (~ 40 MJ energy release), the impurity seeded ELM frequency must increase by at least 40 times compared to the natural ELM frequency. Our simulations have demonstrated that higher impurity density levels

accelerate ELM crash while reducing its size. The ELM frequency upper limit may be determined by the mode growth rate, which triggers ELM crash as MHD instabilities approach saturation and is strongly modulated by impurity induced pedestal profile modifications. Developing multi-ELM cycle simulation is essential for reliable ELM mitigation predictions, a key focus of future work.

6. Conclusion

In this work, we study the nonlinear dynamics of ELM crashes under various impurity seeding scenarios using NIMROD simulations. The characteristic features of ELM crash—filamentary structures, plasma pedestal collapse, and energy loss—are reproduced and agree with experimental observations. The high- n ballooning mode instability, primarily driven by the pedestal pressure gradient, is identified as the most unstable mode and the dominant trigger of ELM crash in this pressure-limited pedestal equilibrium. Impurity seeding significantly influences ELM dynamics by modifying the pedestal pressure profile. The perturbed local pressure gradient drives early-stage mode growth, whereas the subsequent exponential growth of the high- n ballooning mode directly correlates with the maximum flux-surface-averaged pressure gradient. Consequently, higher impurity density levels accelerate ELM crash onset and reduce ELM size. Furthermore, the poloidal location of impurity seeding plays a critical role in ELM crash onset and size: the outboard mid-plane seeding is identified as the most effective trigger for ELM crash, and the lower X-point seeding produces the largest ELM size.

Acknowledgments

We are grateful for the supports from the NIMROD team and the CFETR physics design team. This work was supported by the National Magnetic Confinement Fusion Program of China (Grant No. 2019YFE03050004), Hubei International Science and Technology Cooperation Projects (No. 2022EHB003), and U.S. Department of Energy (Grant No. DE-FG02-86ER53218). The computing work in this paper was supported by the Public Service Platform of High Performance Computing by Network and Computing Center of HUST, and this research used resources of the National Energy Research Scientific Computing Center, a DOE Office of Science User Facility supported by the Office of Science of the U.S. Department of Energy under Contract No. DE-AC02-05CH11231 using NERSC award FES-ERCAP0027638.

References

- [1] Wagner F, Becker G, Behringer K, Campbell D, Eberhagen A, Engelhardt W, Fussmann G, Gehre O, Gernhardt J, Gierke G v, Haas G, Huang M, Karger F, Keilhacker M, Klüber O, Kornherr M, Lackner K, Lisitano G, Lister G G, Mayer H M, Meisel D, Müller E R, Murmann H, Niedermeyer H, Poschenrieder W, Rapp H, Röhr H, Schneider F, Siller G, Speth E, Stäbler A, Steuer K H, Venus G, Vollmer O and Yü Z 1982 Physical Review Letters **49**(19) 1408–1412 URL <https://link.aps.org/doi/10.1103/PhysRevLett.49.1408>
- [2] Loarte A, Saibene G, Sartori R, Becoulet M, Horton L, Eich T, Herrmann A, Laux M, Matthews G, Jachmich S, Asakura N, Chankin A, Leonard A, Porter G, Federici G, Shimada M, Sugihara M and Janeschitz G 2003 Journal of Nuclear Materials **313-316** 962–966 ISSN 0022-3115 plasma-Surface Interactions in Controlled Fusion Devices 15 URL <https://www.sciencedirect.com/science/article/pii/S0022311502013983>
- [3] Zhuang G, Li G, Li J, Wan Y, Liu Y, Wang X, Song Y, Chan V, Yang Q, Wan B, Duan X, Fu P, Xiao B and the CFETR Design Team 2019 Nuclear Fusion **59** 112010 URL <https://dx.doi.org/10.1088/1741-4326/ab0e27>
- [4] Ueda Y, Schmid K, Balden M, Coenen J, Loewenhoff T, Ito A, Hasegawa A, Hardie C, Porton M and Gilbert M 2017 Nuclear Fusion **57** 092006 URL <https://dx.doi.org/10.1088/1741-4326/aa6b60>
- [5] Wade M R, Burrell K H, Leonard A W, Osborne T H and Snyder P B 2005 Physical Review Letters **94**(22) 225001 URL <https://link.aps.org/doi/10.1103/PhysRevLett.94.225001>
- [6] Kirk A, Koch B, Scannell R, Wilson H R, Counsell G, Dowling J, Herrmann A, Martin R and Walsh M (the MAST team) 2006 Physical Review Letters **96**(18) 185001 URL <https://link.aps.org/doi/10.1103/PhysRevLett.96.185001>
- [7] Lang P, Loarte A, Saibene G, Baylor L, Becoulet M, Cavinato M, Clement-Lorenzo S, Daly E, Evans T, Fenstermacher M, Gribov Y, Horton L, Lowry C, Martin Y, Neubauer O, Oyama N, Schaffer M, Stork D, Suttrop W, Thomas P, Tran M, Wilson H, Kavin A and Schmitz O 2013 Nuclear Fusion **53** 043004 URL <https://dx.doi.org/10.1088/0029-5515/53/4/043004>
- [8] Loarte A, Huijsmans G, Futatani S, Baylor L, Evans T, Orlov D M, Schmitz O, Becoulet M, Cahyna P, Gribov Y, Kavin A, Naik A S, Campbell D, Casper T, Daly E, Frerichs H, Kischner A, Laengner R, Lisgo S, Pitts R, Saibene G and Wingen A 2014 Nuclear Fusion **54** 033007 URL <https://dx.doi.org/10.1088/0029-5515/54/3/033007>
- [9] Leonard A W 2014 Physics of Plasmas **21** 090501 ISSN 1070-664X URL <https://doi.org/10.1063/1.4894742>
- [10] Kirk A, Dunai D, Dunne M, Huijsmans G, Pamela S, Becoulet M, Harrison J, Hillesheim J, Roach C and Saarelma S 2014 Nuclear Fusion **54** 114012 URL <https://dx.doi.org/10.1088/0029-5515/54/11/114012>
- [11] Huijsmans G T A, Chang C S, Ferraro N, Sugiyama L, Waelbroeck F, Xu X Q, Loarte A and Futatani S 2015 Physics of Plasmas **22** 021805 ISSN 1070-664X URL <https://doi.org/10.1063/1.4905231>
- [12] Xiao G L, Zhong W L, Zhang Y P, Zou X L, Liang A S, Feng B B, Bai X Y, Zhang K, Mazon D, Chen C Y, Chen W, Cheng J, Delpech L, Ding X T, Dong C F, Dong J Q, Cui Z Y, Ekedahl A, Gao J M, Giruzzi G, Goniche M, Han M K, He X X, Hoang T, Huang Z H, Isobe M, Ji X Q, Li Y G, Liu A D, Liu C H, Liu L, Lu B, Peysson Y, Shi P W, Song X M, Sun P, Wang T B, Wang Z H, Wang Z X, Wen J, Xiao W W, Yan L W, Yang Z C, Yu D L, Yuan G L, Zhang P F, Zhou Y, Shi Z B, Liu Y, Yang Q W, Xu M, Duan X R and the HL-2A team 2020 Journal of Fusion Energy **39** 300–312 URL <https://link.springer.com/article/10.1007/s10894-021-00281-w#Abs1>
- [13] Xu G S, Wang Y F, Yang Q Q, Lin X, Chen R, Ye Y, Lan H and Yan N 2023 Reviews of Modern Plasma Physics **7** URL <https://link.springer.com/article/10.1007/s41614-023-00119-2#citeas>

- [14] Snyder P B, Wilson H R, Ferron J R, Lao L L, Leonard A W, Osborne T H, Turnbull A D, Mossessian D, Murakami M and Xu X Q 2002 Physics of Plasmas **9** 2037–2043 ISSN 1070-664X URL <https://doi.org/10.1063/1.1449463>
- [15] Kleiner A, Ferraro N, Diallo A and Canal G 2021 Nuclear Fusion **61** 064002 URL <https://dx.doi.org/10.1088/1741-4326/abf416>
- [16] Nyström H, Frassinetti L, Saarelma S, Huijsmans G, von Thun C P, Maggi C, Hillesheim J and contributors J 2022 Nuclear Fusion **62** 126045 URL <https://dx.doi.org/10.1088/1741-4326/ac9701>
- [17] Wilson H R and Cowley S C 2004 Physical Review Letters **92**(17) 175006 URL <https://link.aps.org/doi/10.1103/PhysRevLett.92.175006>
- [18] Ham C J, Cowley S C, Brochard G and Wilson H R 2016 Physical Review Letters **116**(23) 235001 URL <https://link.aps.org/doi/10.1103/PhysRevLett.116.235001>
- [19] Diallo A, Dominski J, Barada K, Knolker M, Kramer G J and McKee G 2018 Physical Review Letters **121**(23) 235001 URL <https://link.aps.org/doi/10.1103/PhysRevLett.121.235001>
- [20] Beurskens M, Arnoux G, Brezinsek A, Challis C, de Vries P, Giroud C, Huber A, Jachmich S, McCormick K, Pitts R, Rimini F, Alfier A, de la Luna E, Fundamenski W, Gerasimov S, Giovannozzi E, Joffrin E, Kempenaars M, Litaudon X, Loarer T, Lomas P, Mailloux J, Pasqualotto R, Pericoli-Ridolfini V, Pugno R, Rachlew E, Saarelma S, Solano E, Walsh M, Zabeo L, Zastrow K D and Contributors J E 2008 Nuclear Fusion **48** 095004 URL <https://dx.doi.org/10.1088/0029-5515/48/9/095004>
- [21] Schneider P A, Wolfrum E, Dunne M G, Dux R, Gude A, Kurzan B, Pütterich T, Rathgeber S K, Vicente J, Weller A, Wenninger R and the ASDEX Upgrade Team 2014 Plasma Physics and Controlled Fusion **56** 025011 URL <https://dx.doi.org/10.1088/0741-3335/56/2/025011>
- [22] Li K, Xu G, Yang Z, Wang L, Yuan Q, Liu J, Wang H, Guo H, Eldon D, Hyatt A, Humphreys D, Yang Q, Lin X, Xu J, Meng L, Ding F, Chen X, Wu J, Wu K, Duan Y and Luo G N 2020 Plasma Physics and Controlled Fusion **62** 095025 URL <https://dx.doi.org/10.1088/1361-6587/aba859>
- [23] Lin X, Xu G, Yang Q, Yan N, Wang Y, Ye Y, Zhu P, Cao B, Li K, Chen R, Zhang L, Zang Q, Zhang T, Wang Y, Hu G, Li Y, Zhou C, Chen Y, Meng L, Yang X, Duan Y, Liu H, Ding F, Chen X, Xu J, Wu M and Wang L 2022 Physics Letters A **431** 127988 ISSN 0375-9601 URL <https://www.sciencedirect.com/science/article/pii/S0375960122000706>
- [24] Xiao W, Diamond P, Zou X, Dong J, Ding X, Yao L, Feng B, Chen C, Zhong W, Xu M, Yuan B, Rhee T, Kwon J, Shi Z, Rao J, Lei G, Cao J, Zhou J, Huang M, Yu D, Huang Y, Zhao K, Cui Z, Song X, Gao Y, Zhang Y, Cheng J, Han X, Zhou Y, Dong Y, Ji X, Yang Q, Liu Y, Yan L, Duan X, Liu Y and the HL-2A Team 2012 Nuclear Fusion **52** 114027 URL <https://dx.doi.org/10.1088/0029-5515/52/11/114027>
- [25] Zhong W, Zou X, Feng B, Xiao G, Liang A, Yang Z, Chen C, Gao J, Cheng J, Zhang Y, Wang T, Han M, Wang Z, Xiao W, Liu L, Jiang M, Shi P, Wen J, Cui Z, Dong C, Liu C, Wang Z, Song X, Yan L, Dong J, Ding X, Yu D, Shi Z, Liu Y, Yang Q, Xu M, Duan X and the HL-2A team 2019 Nuclear Fusion **59** 076033 URL <https://dx.doi.org/10.1088/1741-4326/ab1d7a>
- [26] Xiao W, Diamond P, Kim W, Yao L, Yoon S, Ding X, Hahn S, Kim J, Xu M, Chen C, Feng B, Cheng J, Zhong W, Shi Z, Jiang M, Han X, Nam Y, Ko W, Lee S, Bak J, Ahn J, Kim H, Kim H, Kim K, Zou X, Song S, Song J, Yu Y, Rhee T, Kwon J, Huang X, Yu D, Lee K, Park S, Jung M, Zoletnik S, Lampert M, Tynan G, Bae Y, Kwak J, Yan L, Duan X, Oh Y, Dong J, the KSTAR Team and the HL-2A Team 2014 Nuclear Fusion **54** 023003 URL <https://dx.doi.org/10.1088/0029-5515/54/2/023003>
- [27] Zhang Y, Mazon D, Zou X, Zhong W, Gao J, Zhang K, Sun P, Dong C, Cui Z, Liu Y, Shi Z, Yu D, Cheng J, Jiang M, Xu J, Isobe M, Xiao G, Chen W, Song S, Bai X, Zhang P, Yuan G, Ji X, Li Y, Zhou Y, Delpech L, Ekedahl A, Giruzzi G, Hoang T, Peysson Y, Song X, Song X, Li X, Ding X, Dong J, Yang Q, Xu M, Duan X, Liu Y and the HL-2A team 2018 Nuclear Fusion **58** 046018 URL <https://dx.doi.org/10.1088/1741-4326/aaae81>

- [28] Xiao G, Zou X, Zhong W, Xu M, Zhang Y, Mazon D, Dong C, Dong J, Fang K, Feng B, Gao J, Han M, He X, Li J, Li Y, Liang A, Song X, Shi Z, Sun P, Wen J, Yang Z, Yu D, Zhang K, Duan X and Team H A 2021 Nuclear Fusion **61** 116011 URL <https://dx.doi.org/10.1088/1741-4326/ac1c87>
- [29] Sun Z, Qian Y, Maingi R, Wang Y, Wang Y, Nagy A, Tritz K, Lunsford R, Gilson E, Zuo G, Xu W, Huang M, Meng X, Mansfield D, Zang Q, Zhu X, Lin X, Liu H, Duan Y, Zhang L, Lyu B, Liu Y, Wang L, Bortolon A, Xu G, Gong X, Hu J and the EAST team 2021 Nuclear Fusion **61** 066022 URL <https://dx.doi.org/10.1088/1741-4326/abf855>
- [30] Sun Z, Diallo A, Maingi R, Qian Y, Tritz K, Wang Y, Wang Y, Bortolon A, Nagy A, Zhang L, Duan Y, Ye Y, Zhao H, Wang H, Gu X, Zuo G, Xu W, Huang M, Li C, Meng X, Zhou C, Liu H, Zang Q, Wang L, Qian J, Xu G, Gong X, Hu J and team E 2020 Nuclear Fusion **61** 014002 URL <https://dx.doi.org/10.1088/1741-4326/abc763>
- [31] Ye Y, Xu G, Tao Y, Chen R, Wang L, Guo H, Wang H, Li K, Meng L, Yang Q, Wang Y, Lin X, Sun Z, Wu K, Yuan Q, Xu J, Duan Y, Zhang L, Liu H and Wan B 2021 Nuclear Fusion **61** 116032 URL <https://dx.doi.org/10.1088/1741-4326/ac26eb>
- [32] Baylor L R, Commaux N, Jernigan T C, Brooks N H, Combs S K, Evans T E, Fenstermacher M E, Isler R C, Lasnier C J, Meitner S J, Moyer R A, Osborne T H, Parks P B, Snyder P B, Strait E J, Unterberg E A and Loarte A 2013 Physical Review Letters **110**(24) 245001 URL <https://link.aps.org/doi/10.1103/PhysRevLett.110.245001>
- [33] Baylor L R, Commaux N, Jernigan T C, Meitner S J, Combs S K, Isler R C, Unterberg E A, Brooks N H, Evans T E, Leonard A W, Osborne T H, Parks P B, Snyder P B, Strait E J, Fenstermacher M E, Lasnier C J, Moyer R A, Loarte A, Huijsmans G T A and Futatani S 2013 Physics of Plasmas **20** 082513 ISSN 1070-664X URL <https://doi.org/10.1063/1.4818772>
- [34] Wilcox R, Baylor L, Bortolon A, Knolker M, Lasnier C, Shiraki D, Bykov I, Chrystal C, Scotti F, Paz-Soldan C and Wingen A 2021 Nuclear Fusion **62** 026017 URL <https://dx.doi.org/10.1088/1741-4326/ac3b8b>
- [35] Lang P, Alonso A, Alper B, Belonohy E, Boboc A, Devaux S, Eich T, Frigione D, Gál K, Garzotti L, Geraud A, Kocsis G, Köchl F, Lackner K, Loarte A, Lomas P, Maraschek M, Müller H, Neu R, Neuhauser J, Petravich G, Saibene G, Schweinzer J, Thomsen H, Tsalias M, Wenninger R, Zohm H and Contributors J E 2011 Nuclear Fusion **51** 033010 URL <https://dx.doi.org/10.1088/0029-5515/51/3/033010>
- [36] Lang P, Frigione D, Géraud A, Alarcon T, Bennett P, Cseh G, Garnier D, Garzotti L, Köchl F, Kocsis G, Lennholm M, Neu R, Mooney R, Saarelma S, Sieglin B and Contributors J E 2013 Nuclear Fusion **53** 073010 URL <https://dx.doi.org/10.1088/0029-5515/53/7/073010>
- [37] Lang P, Conway G, Eich T, Fattorini L, Gruber O, Günter S, Horton L, Kalvin S, Kallenbach A, Kaufmann M, Kocsis G, Lorenz A, Manso M, Maraschek M, Mertens V, Neuhauser J, Nunes I, Schneider W, Suttrop W, Urano H and the ASDEX Upgrade Team 2004 Nuclear Fusion **44** 665 URL <https://dx.doi.org/10.1088/0029-5515/44/5/010>
- [38] Kocsis G, Kálvin S, Lang P, Maraschek M, Neuhauser J, Schneider W, Szepesi T and the ASDEX Upgrade Team 2007 Nuclear Fusion **47** 1166 URL <https://dx.doi.org/10.1088/0029-5515/47/9/013>
- [39] Xu X Q, Dudson B, Snyder P B, Umansky M V and Wilson H 2010 Physical Review Letters **105**(17) 175005 URL <https://link.aps.org/doi/10.1103/PhysRevLett.105.175005>
- [40] Dudson B D, Xu X Q, Umansky M V, Wilson H R and Snyder P B 2011 Plasma Physics and Controlled Fusion **53** 054005 URL <https://dx.doi.org/10.1088/0741-3335/53/5/054005>
- [41] Wu N, Chen S Y, Mou M L and Tang C J 2018 Physics of Plasmas **25** 092305 ISSN 1070-664X URL <https://doi.org/10.1063/1.5038042>
- [42] Wingen A, Wilcox R, Lyons B, Baylor L and Ferraro N 2024 Nuclear Fusion **64** 066015 URL <https://dx.doi.org/10.1088/1741-4326/ad3f30>
- [43] Orain F, Bécoulet M, Huijsmans G T A, Dif-Pradalier G, Hoelzl M, Morales J, Garbet X, Nardon E, Pamela S, Passeron C, Latu G, Fil A and Cahyna P 2015 Physical Review Letters **114**(3)

- 035001 URL <https://link.aps.org/doi/10.1103/PhysRevLett.114.035001>
- [44] Cathey A, Hoelzl M, Lackner K, Huijsmans G, Dunne M, Wolfrum E, Pamela S, Orain F, Günter S, the JOEREK team, the ASDEX Upgrade team and the EUROfusion MST1 team 2020 Nuclear Fusion **60** 124007 URL <https://dx.doi.org/10.1088/1741-4326/abbc87>
 - [45] Cathey A, Hoelzl M, Harrer G, Dunne M G, Huijsmans G T A, Lackner K, Pamela S J P, Wolfrum E, Günter S, the JOEREK Team, the ASDEX Upgrade Team and the EUROfusion MST1 Team 2022 Plasma Physics and Controlled Fusion **64** 054011 URL <https://dx.doi.org/10.1088/1361-6587/ac5b4b>
 - [46] Huijsmans G T A, Pamela S, van der Plas E and Ramet P 2009 Plasma Physics and Controlled Fusion **51** 124012 URL <https://dx.doi.org/10.1088/0741-3335/51/12/124012>
 - [47] Futatani S, Pamela S, Garzotti L, Huijsmans G, Hoelzl M, Frigione D, Lennholm M, the JOEREK Team and Contributors J 2019 Nuclear Fusion **60** 026003 URL <https://dx.doi.org/10.1088/1741-4326/ab56c7>
 - [48] Cathey A, Hoelzl M, Futatani S, Lang P T, Lackner K, Huijsmans G T A, Pamela S J P, Günter S, the JOEREK Team, the ASDEX Upgrade Team and the EUROfusion MST1 Team 2021 Plasma Physics and Controlled Fusion **63** 075016 URL <https://dx.doi.org/10.1088/1361-6587/abf80b>
 - [49] Futatani S, Cathey A, Hoelzl M, Lang P, Huijsmans G, Dunne M, the JOEREK Team, the ASDEX Upgrade Team and the EUROfusion MST1 Team 2021 Nuclear Fusion **61** 046043 URL <https://dx.doi.org/10.1088/1741-4326/abdfb4>
 - [50] Burke B J, Kruger S E, Hegna C C, Zhu P, Snyder P B, Sovinec C R and Howell E C 2010 Physics of Plasmas **17** 032103 ISSN 1070-664X URL <https://doi.org/10.1063/1.3309732>
 - [51] Brennan D P, Kruger S E, Schnack D D, Sovinec C R and Pankin A 2006 Journal of Physics: Conference Series **46** 63 URL <https://dx.doi.org/10.1088/1742-6596/46/1/009>
 - [52] Sovinec C R, Barnes D C, Bayliss R A, Brennan D P, Held E D, Kruger S E, Pankin A Y, Schnackand D D and the NIMROD Team 2007 Journal of Physics: Conference Series **78** 012070 URL <https://dx.doi.org/10.1088/1742-6596/78/1/012070>
 - [53] Zhu P, Hegna C C and Sovinec C R 2012 Physics of Plasmas **19** 032503 ISSN 1070-664X URL <https://doi.org/10.1063/1.3692089>
 - [54] Banerjee D, Zhu P and Maingi R 2017 Nuclear Fusion **57** 076005 URL <https://dx.doi.org/10.1088/1741-4326/aa6b25>
 - [55] Lin X, Banerjee D, Zhu P, Xu G S, Ye Y, Wang Y F, Li H L, Zang Q, Zhang T and Chen Y J 2020 Plasma Physics and Controlled Fusion **62** 035011 URL <https://dx.doi.org/10.1088/1361-6587/ab6d47>
 - [56] Pankin A, King J, Kruger S, Chen X, Burrell K, Garofalo A, Groebner R J, McKee G and Yan Z 2020 Nuclear Fusion **60** 092004 URL <https://dx.doi.org/10.1088/1741-4326/ab9afe>
 - [57] Lunsford R, Sun Z, Maingi R, Hu J, Mansfield D, Xu W, Zuo G, Diallo A, Osborne T, Tritz K, Canik J, Huang M, Meng X, Gong X, Wan B, Li J and the EAST team 2018 Nuclear Fusion **58** 036007 URL <https://dx.doi.org/10.1088/1741-4326/aaa2ac>
 - [58] Futatani S, Huijsmans G, Loarte A, Baylor L, Commaux N, Jernigan T, Fenstermacher M, Lasnier C, Osborne T and Pegourié B 2014 Nuclear Fusion **54** 073008 URL <https://dx.doi.org/10.1088/0029-5515/54/7/073008>
 - [59] Maingi R, Kaye S M, Skinner C H, Boyle D P, Canik J M, Bell M G, Bell R E, Gray T K, Jaworski M A, Kaita R, Kugel H W, LeBlanc B P, Mansfield D K, Osborne T H, Sabbagh S A and Soukhanovskii V A 2011 Physical Review Letters **107**(14) 145004 URL <https://link.aps.org/doi/10.1103/PhysRevLett.107.145004>
 - [60] Harrer G, Wolfrum E, Dunne M, Manz P, Cavedon M, Lang P, Kurzan B, Eich T, Labit B, Stober J, Meyer H, Bernert M, Laggner F, Aumayr F, the EUROfusion MST1 Team and the ASDEX Upgrade Team 2018 Nuclear Fusion **58** 112001 URL <https://dx.doi.org/10.1088/1741-4326/aad757>
 - [61] Dunne M G, Potzel S, Reimold F, Wischmeier M, Wolfrum E, Frassinetti L, Beurskens M, Bilkova

- P, Cavedon M, Fischer R, Kurzan B, Laggner F M, McDermott R M, Tardini G, Trier E, Viezzer E, Willensdorfer M, Team T E M and Team T A U 2016 Plasma Physics and Controlled Fusion **59** 014017 URL <https://dx.doi.org/10.1088/0741-3335/59/1/014017>
- [62] Sovinec C R, Glasser A H, Gianakon T A, Barnes D C, Nebel R A, Kruger S E, Schnack D D, Plimpton S J, Tarditi A and Chu M S 2004 Journal of Computational Physics **195** 355–386 ISSN 00219991 URL <https://www.sciencedirect.com/science/article/pii/S0021999103005369>
- [63] Whyte D G, Evans T E, Kellman A G, Humphreys D A, Hyatt A W, Jernigan T C, Lee R L, Luckhardt S L, Parks P B, Schaffer M J and Taylor P L Proceedings of the 24th European Conference on Controlled Fusion and Plasma Physics, 9–14 June 1996, Berchtesgaden, Germany(European Physical Society, Geneva, 1997) **21A** p. 1137 URL http://libero.ipp.mpg.de/libero/PDF/EPS_24_Vol3_1997.pdf
- [64] Izzo V A 2013 Physics of Plasmas **20** 056107 ISSN 1070-664X URL <https://doi.org/10.1063/1.4803896>
- [65] Groebner R J and Saarelma S 2023 Plasma Physics and Controlled Fusion **65** 073001 URL <https://dx.doi.org/10.1088/1361-6587/acd478>
- [66] Kirk A, Counsell G F, Cunningham G, Dowling J, Dunstan M, Meyer H, Price M, Saarelma S, Scannell R, Walsh M, Wilson H R and the MAST team 2007 Plasma Physics and Controlled Fusion **49** 1259 URL <https://dx.doi.org/10.1088/0741-3335/49/8/011>
- [67] Yun G S, Lee W, Choi M J, Lee J, Park H K, Tobias B, Domier C W, Luhmann N C, Donné A J H and Lee J H (KSTAR Team) 2011 Physical Review Letters **107**(4) 045004 URL <https://link.aps.org/doi/10.1103/PhysRevLett.107.045004>
- [68] Saarelma S, Hender T C, Kirk A, Meyer H, Wilson H R and Team M 2006 Plasma Physics and Controlled Fusion **49** 31 URL <https://dx.doi.org/10.1088/0741-3335/49/1/003>
- [69] Huysmans G and Czarny O 2007 Nuclear Fusion **47** 659 URL <https://dx.doi.org/10.1088/0029-5515/47/7/016>
- [70] Lang P T, Büchl K, Kaufmann M, Lang R S, Mertens V, Müller H W and Neuhauser J (ASDEX Upgrade and NI Teams) 1997 Physical Review Letters **79**(8) 1487–1490 URL <https://link.aps.org/doi/10.1103/PhysRevLett.79.1487>
- [71] Lennholm M, McKean R, Mooney R, Tvalashvili G, Artaserse G, Baruzzo M, Belonohy E, Calabro G, Carvalho I, Challis C, de la Luna E, Frigione D, Garzotti L, Henriques R, Hobirk J, Jaquet P, Kappatou A, Keeling D, King D, Lang P, Lerche E, Lomas P, Lowry C, Maslov M, Moradi S, Nave M, Nunes I, von Thun C P, Reux C, Rimini F, Sips A, Sozzi C, Valovic M, Eester D V and contributors J 2021 Nuclear Fusion **61** 036035 URL <https://dx.doi.org/10.1088/1741-4326/abd861>

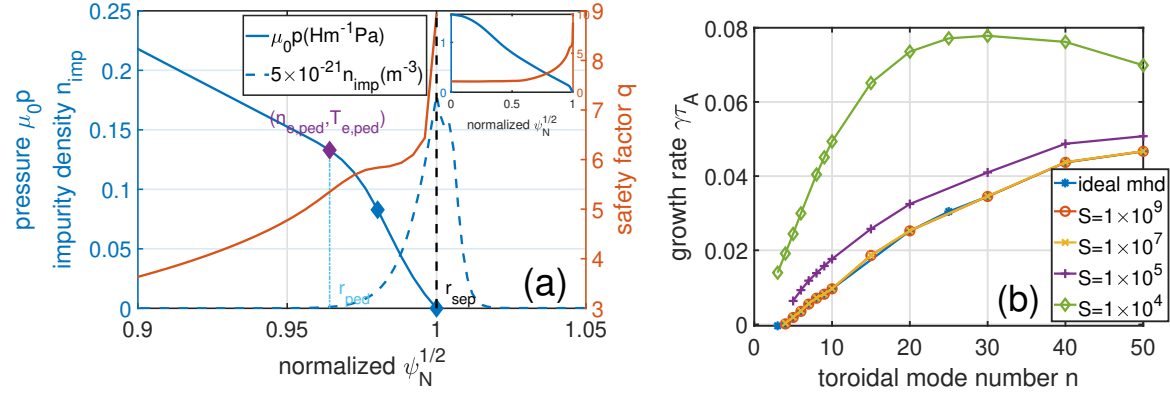


Figure 1: (a) Equilibrium profiles of plasma pressure $\mu_0 p$ (blue solid line) and safety factor q (orange solid line) in the pedestal region, with the plasma separatrix marked using a black dashed line. The locations of pedestal density $n_{e,\text{ped}}$ and temperature $T_{e,\text{ped}}$ are marked using purple diamonds. The impurity ion density profile is shown as a blue dashed line. The top-right inset displays global profiles using the same color schemes. (b) Linear growth rates versus toroidal mode number n for various Lundquist number S regimes from the linear MHD simulations using NIMROD code.

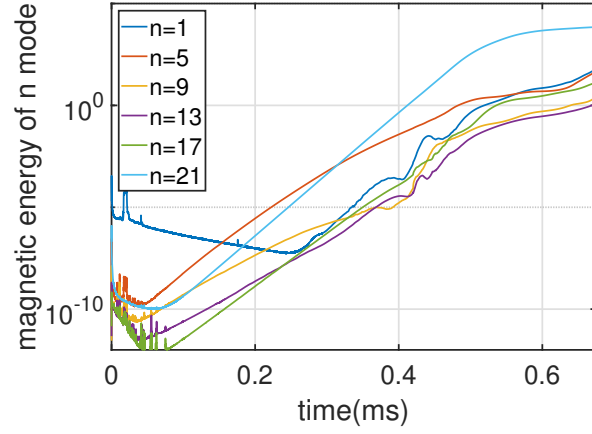


Figure 2: Magnetic energy evolution of selected toroidal modes n versus time, with the Lundquist number in the plasma core region set to $S = 1 \times 10^7$.

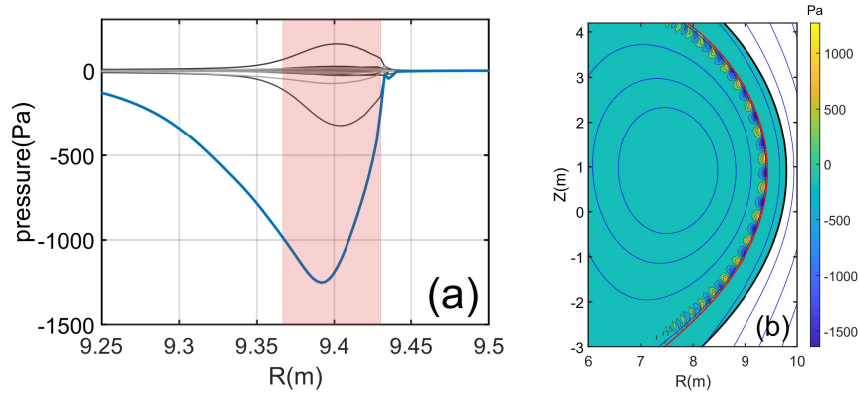


Figure 3: (a) Pressure profiles of selected toroidal mode components at $t = 0.45$ ms, with the $n = 21$ mode (blue line) and the pedestal region (red-shaded area) highlighted. (b) Pressure contour of the toroidal mode $n = 21$ at $t = 0.45$ ms, along with the equilibrium flux surfaces (blue contours) and the plasma separatrix (red line).

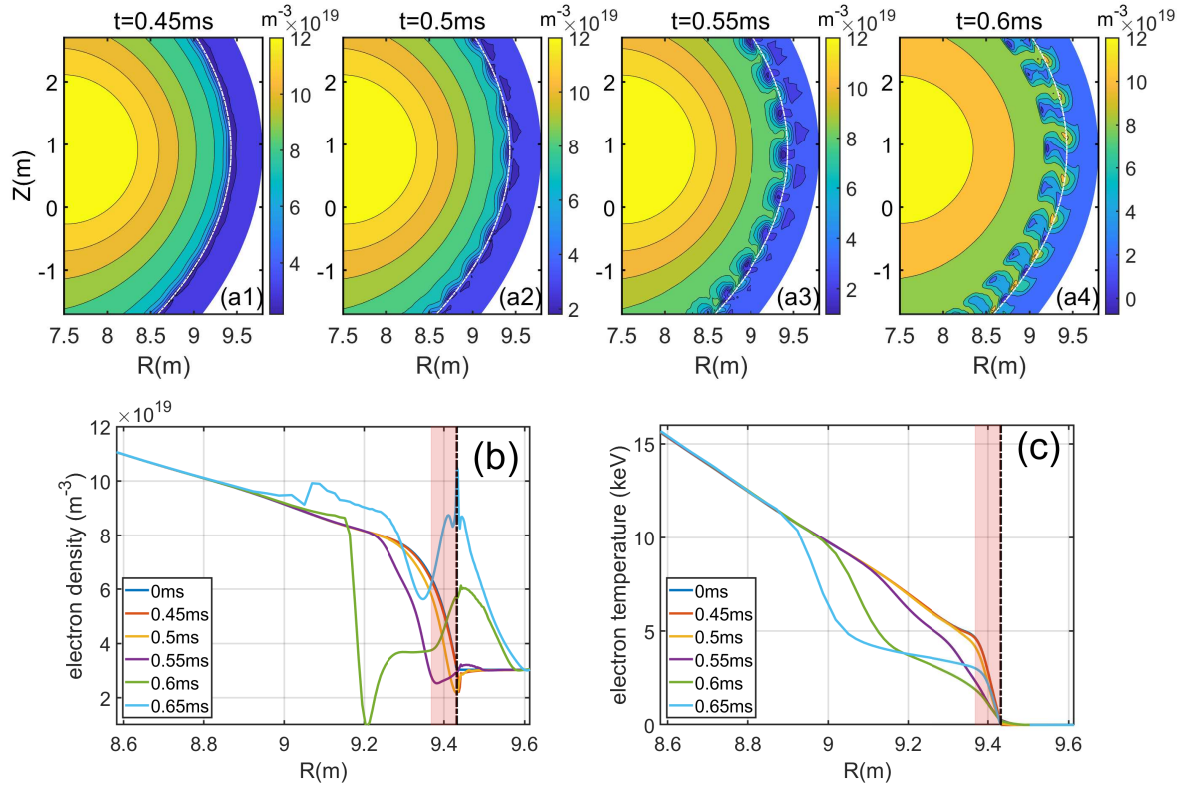


Figure 4: (a1-a4) Electron density contours at $t = 0.45$ ms, 0.5 ms, 0.55 ms, and 0.6 ms, with the plasma separatrix marked using white dashed lines. (b) Outboard mid-plane radial electron density and (c) temperature profiles at a sequence of time. The plasma pedestal region (red-shaded area) and separatrix (black dashed) are highlighted.

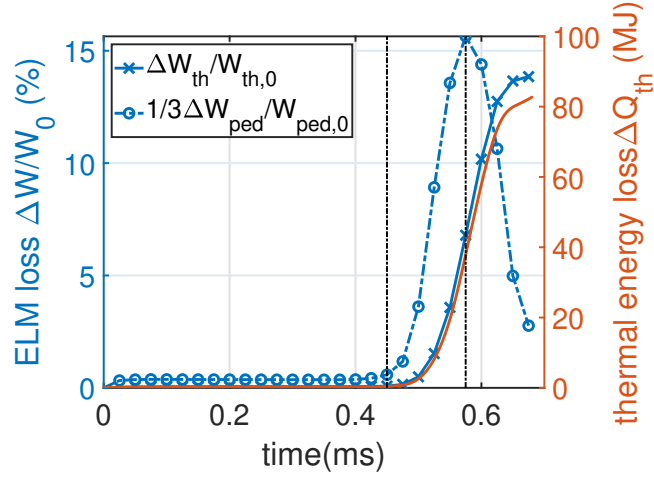


Figure 5: ELM energy losses (blue lines) and the total plasma thermal energy loss ΔQ_{th} (orange solid line) as functions of time. The total ELM loss $\Delta W_{th}/\Delta W_{th,0}$ is defined by $W_{th} = \int 3n_e T_e dS$ (integrated over the entire plasma region), where $W_{th,0}$ denotes the initial total thermal energy and $\Delta W_{th} = W_{th,0} - W_{th}$. The pedestal ELM loss $\Delta W_{ped}/\Delta W_{ped,0}$ is calculated via $W_{ped} = \int_0^{2\pi} d\theta \int_{r_{ped}}^{r_{sep}} 3n_e T_e dr$, limited to the pedestal region between the pedestal top r_{ped} and the plasma separatrix r_{sep} , where $W_{ped,0}$ represents the initial pedestal thermal energy and $\Delta W_{ped} = W_{ped,0} - W_{ped}$.

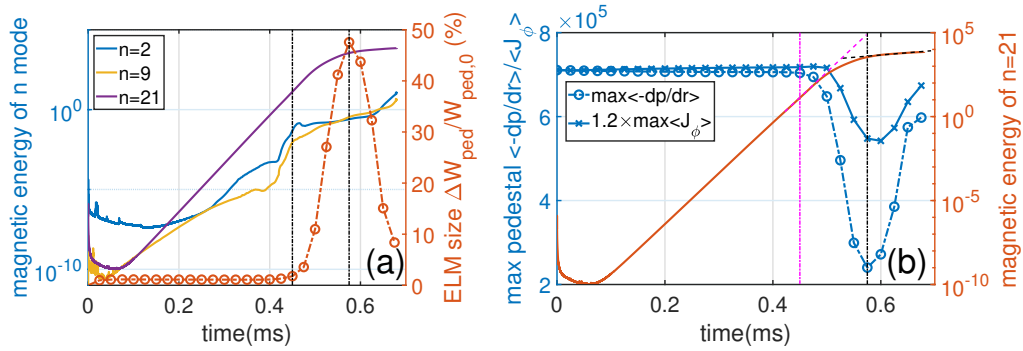


Figure 6: (a) Pedestal ELM size (orange dashed line) and magnetic energies of selected toroidal modes are shown as functions of time. (b) Magnetic energy of toroidal mode $n = 21$ (orange solid line), maximum flux-surface-averaged pedestal pressure gradient (blue dashed line), and its associated toroidal current density (blue solid line) are plotted as functions of time.

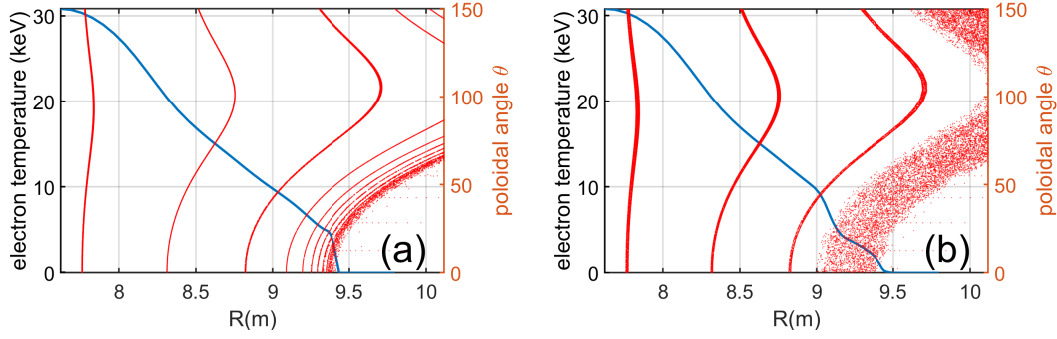


Figure 7: Poincaré plots of magnetic field lines (red dots) and temperature profiles (blue lines) at (a) $t = 0.45$ ms and (b) $t = 0.6$ ms.

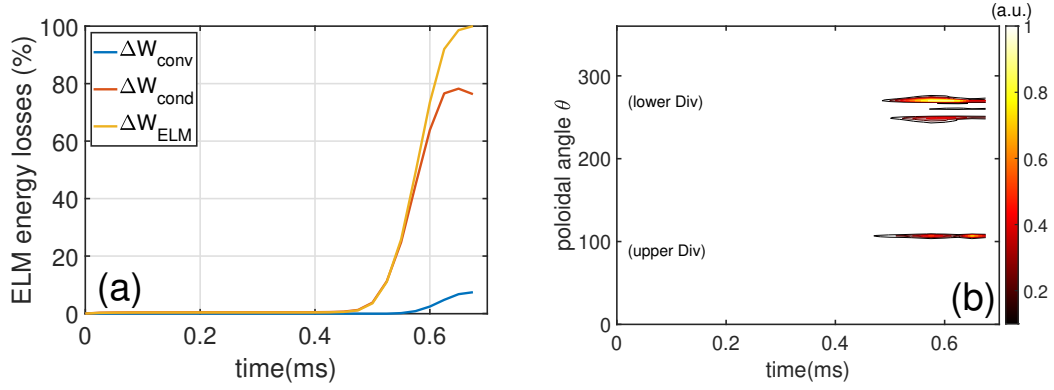


Figure 8: (a) Definitions of energy losses include: convective loss $\Delta W_{conv} = \int \Delta n \langle \Delta T \rangle_t dS$, conductive loss $\Delta W_{cond} = \int \langle \Delta n \rangle_t \Delta T dS$, and total ELM energy loss $\Delta W_{ELM} = \int \Delta n \Delta T dS$, all normalized to $\max(\Delta W_{ELM})$ and shown as functions of time. Here, Δn and ΔT denote instantaneous density and temperature perturbations, respectively, while $\langle \Delta n \rangle_t$ and $\langle \Delta T \rangle_t$ represent their time-averaged counterparts. (b) Normalized heat load distribution on the wall along the poloidal direction as a function of time.

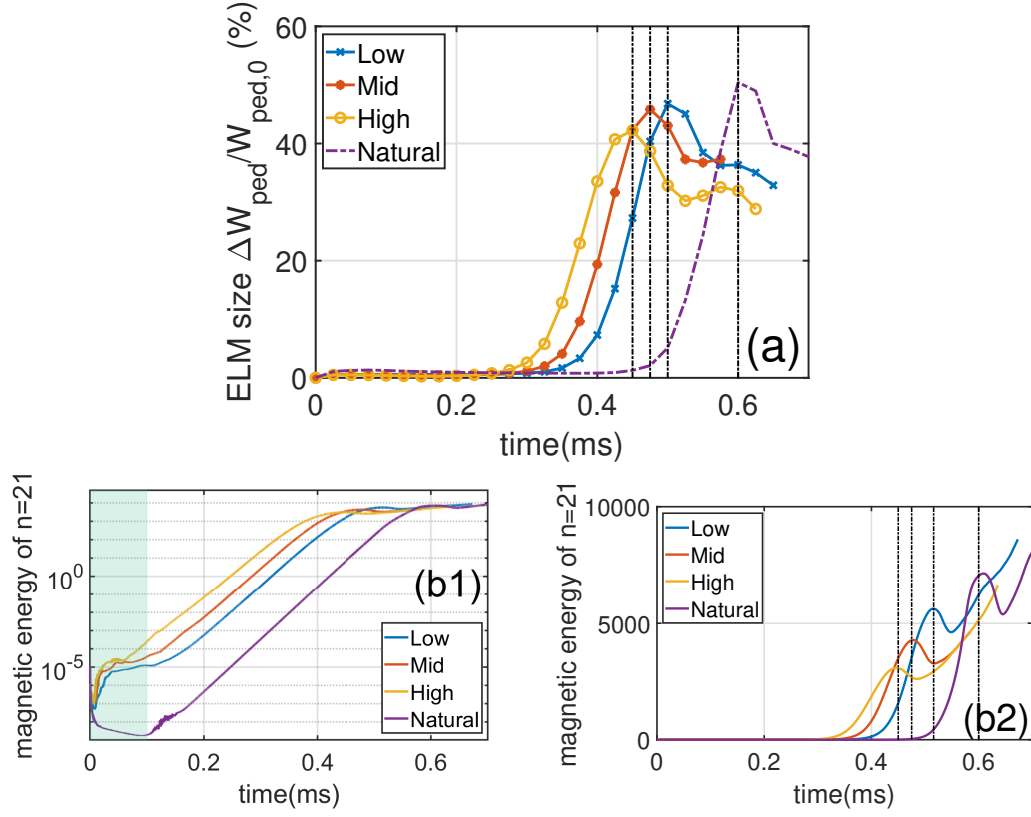


Figure 9: (a) ELM size and (b1-b2) magnetic energy of the $n = 21$ mode are shown as functions of time for various impurity density levels. Cases labeled ‘Low’, ‘Mid’, and ‘High’ correspond to maximum injected impurity ion densities of approximately 1%, 5%, and 10% of the line-averaged plasma density at ELM crash, respectively. ‘Natural’ denotes the reference case without impurity seeding. The Lundquist number in the plasma core is set to $S = 1 \times 10^9$.

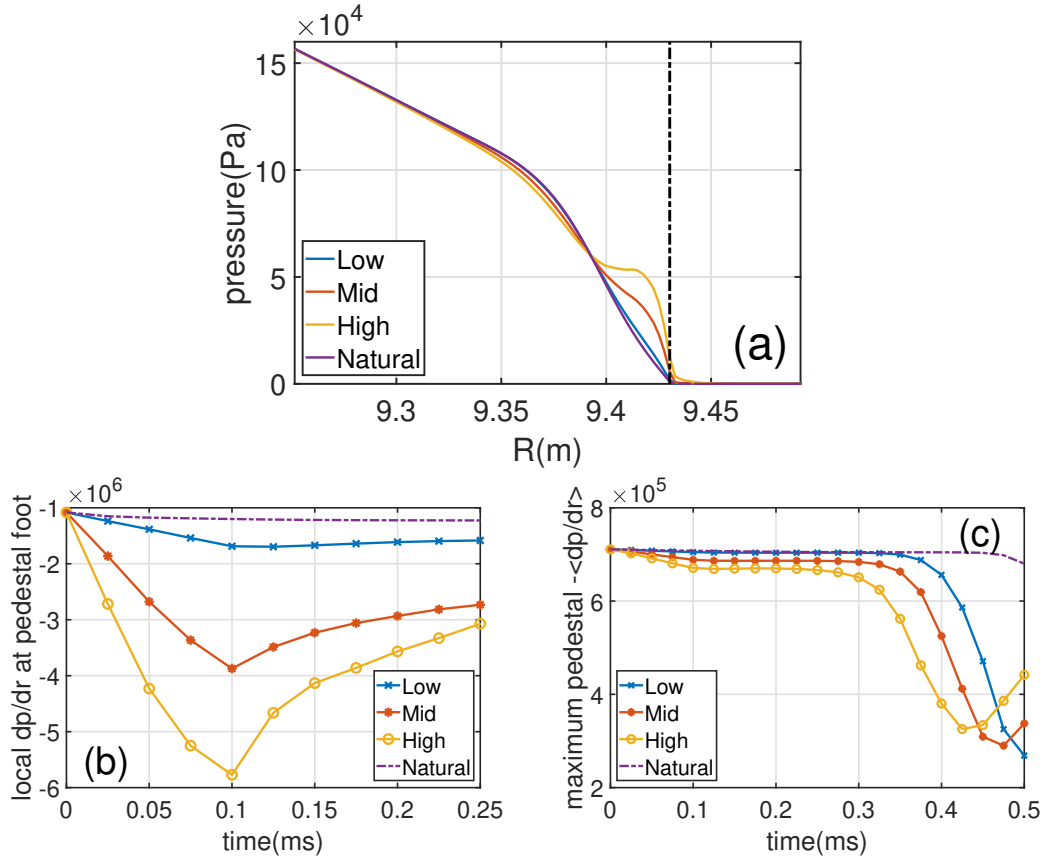


Figure 10: (a) Pedestal pressure profiles on the outboard mid-plane at $t = 0.1$ ms are shown for various impurity density levels. (b) Local pressure gradient at the pedestal foot region on the outboard mid-plane and (c) the maximum flux-surface-averaged pedestal pressure gradient are plotted as functions of time for various impurity density levels.

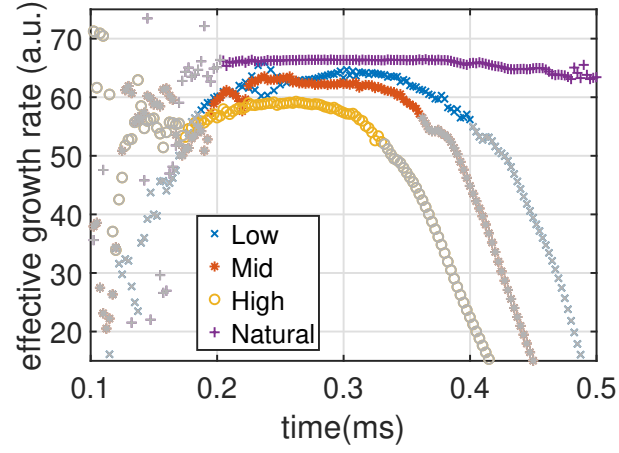


Figure 11: Effective growth rates of the $n = 21$ mode ($d \ln W_{\text{mag},n=21}/dt$, where $W_{\text{mag},n=21}$ denotes the magnetic energy of the $n = 21$ mode) are plotted as a function of time for various impurity density levels.

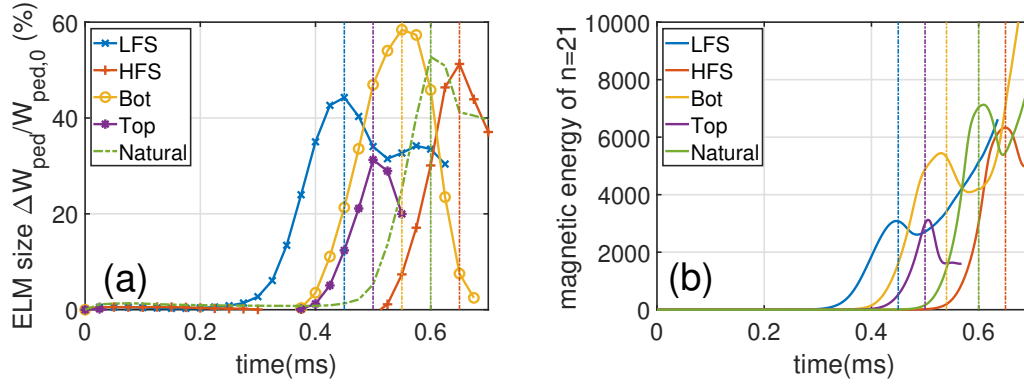


Figure 12: (a) ELM size and (b) magnetic energy of the $n = 21$ mode are shown as functions of time for different poloidal impurity seeding locations. Labels ‘LFS’, ‘HFS’, ‘Bot’, and ‘Top’ correspond to impurity seeding at the outboard mid-plane, inboard mid-plane, lower X-point, and top of the device, respectively. ‘Natural’ denotes the reference case without impurity seeding. The Lundquist number in the plasma core is set to $S = 1 \times 10^9$.

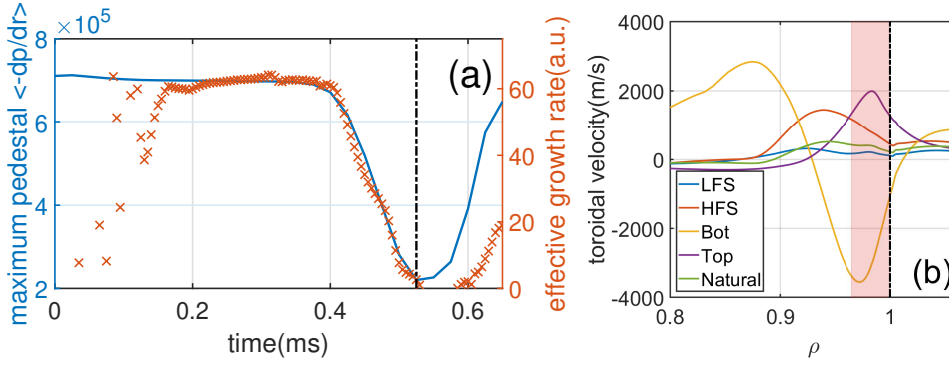


Figure 13: (a) Effective growth rate of the $n = 21$ mode ($d \ln W_{\text{mag}, n=21} / dt$) and the maximum flux-surface-averaged pedestal pressure gradient are plotted as functions of time for the 'Bot' impurity seeding case. (b) Radial profiles of flux-surface-averaged toroidal velocity for various poloidal impurity seeding locations at the time of maximum ELM size.

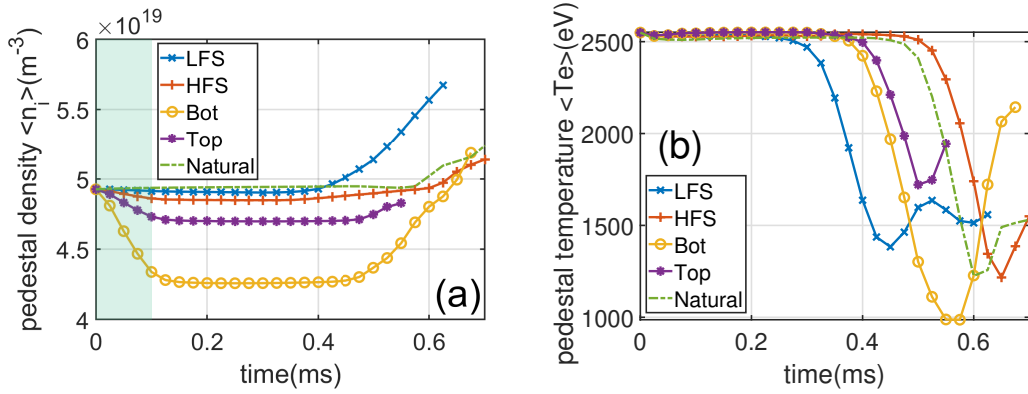


Figure 14: Time evolution of the pedestal-averaged (a) plasma ion density $\langle n_i \rangle = \int_{S_{\text{ped}}} n_i dS / S_{\text{ped}}$ and (b) electron temperature $\langle T_e \rangle = \int_{S_{\text{ped}}} T_e dS / S_{\text{ped}}$ for various poloidal impurity seeding locations, where S_{ped} denotes the poloidal cross-section area of the plasma pedestal region.

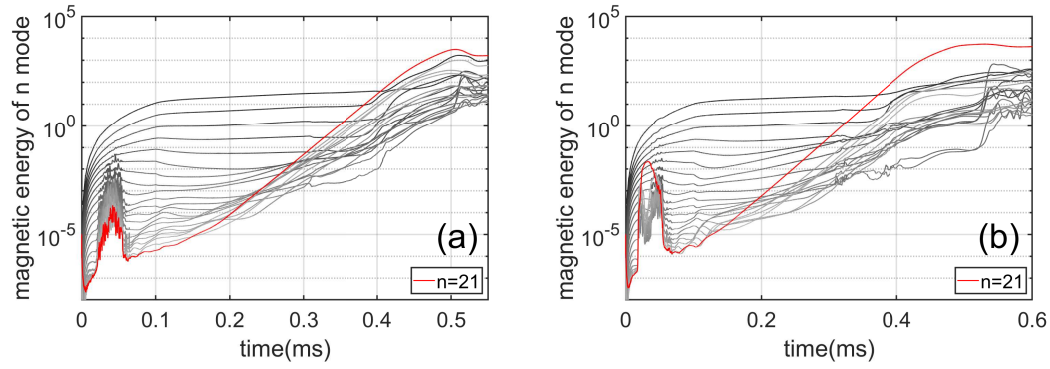


Figure 15: Magnetic energy evolution of selected toroidal modes are shown as functions of time for (a) the 'Top' and (b) the 'Bot' impurity seeding cases, with the $n = 21$ mode (red line) highlighted.

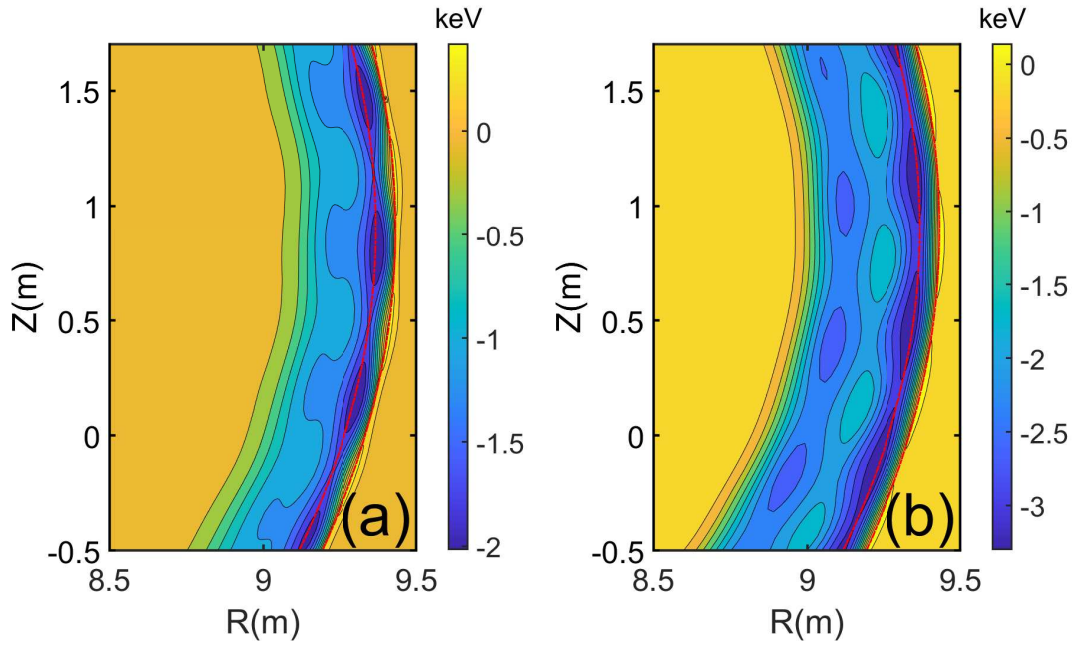


Figure 16: Electron temperature perturbation contours for (a) the 'Top' seeding at $t = 0.5$ ms and (b) the 'Bot' seeding at $t = 0.55$ ms, with the pedestal top and plasma separatrix marked using red dashed lines.

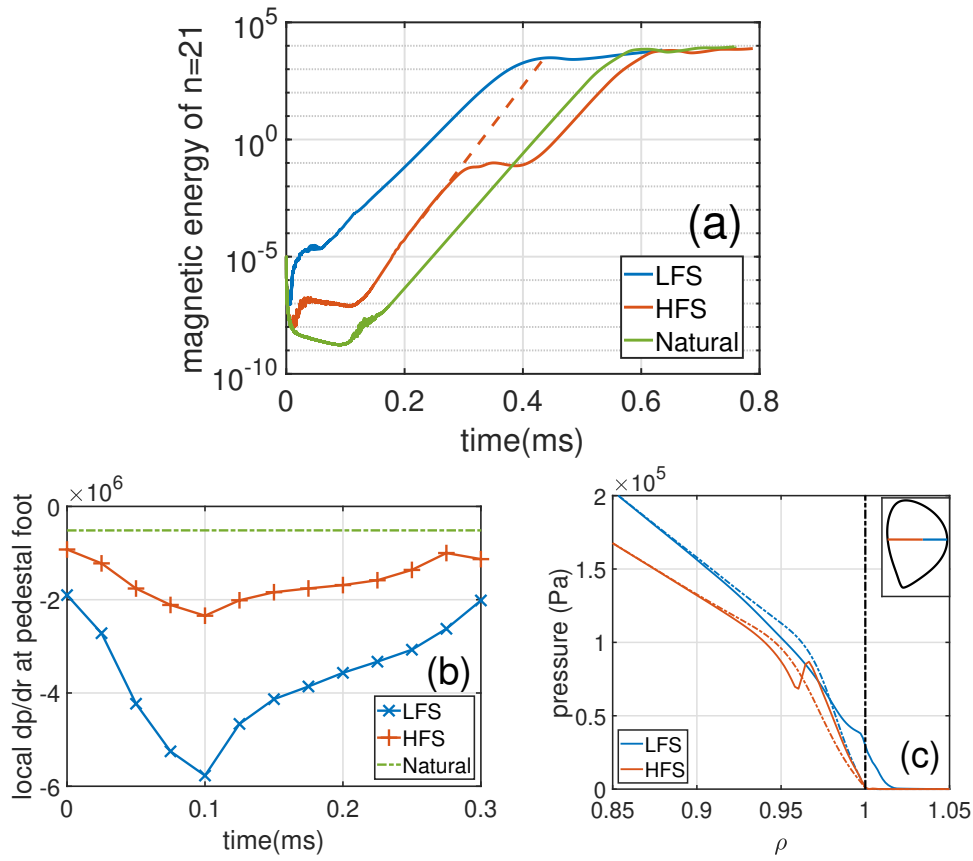


Figure 17: (a) Magnetic energy of the $n = 21$ mode and (b) local pressure gradient at the pedestal foot region are plotted as functions of time for different poloidal impurity seeding locations. (c) Radial pressure profiles at $t = 0.3$ ms along the correspondingly colored radial lines in the top-right inset, with the initial equilibrium represented by dashed lines and the plasma separatrix marked using a black dashed line.